Comparing Transfer Learning to Feature Optimization in Microstructure Classification

Debanshu Banerjee[1] and Taylor D. Sparks*[2]

[1]Metallurgical and Material Engineering Department, Jadavpur University, India
[2]Department of Materials Science and Engineering, The University of Utah, United States of America

August 23, 2021

Abstract

Human analysis of research data is slow and inefficient. In recent years machine learning tools have advanced our capability to perform tasks normally carried out by humans, such as image segmentation and classification. In this work, we seek to further improve binary classification models for high throughput identification of different microstructural morphologies. We utilize a dataset with limited observations (133 dendritic structures, 444 non-dendritic) and employ data augmentation via rotation and translation to enhance the dataset six-fold. Then, transfer learning is carried out using pre-trained networks VGG16, InceptionV3, and Xception achieving only moderate F1 scores (0.801 to 0.822). We hypothesize that feature engineering could yield better results than transfer learning alone. To test this, we employ a new nature-inspired feature optimization algorithm, the Binary Red Deer Algorithm (BRDA), to carry out binary classification and observe F1 scores in the range of 0.96.

1 Introduction

Materials science is centered around the concept of understanding, extracting, and exploiting relationships between structure, property, processing, and characterization of materials. Images of a material's crystal or microstructure can be invaluable in establishing structure-processing-property linkages. However, the human eye itself can only resolve objects as small as $\sim 50\,\mu$m. Investigating smaller details than this requires microscopy like optical microscopy, transmission electron microscopy (TEM), scanning electron microscopy (SEM), atomic force microscopy (AFM), and others. Each of these techniques offers different resolution limitations along with other advantages and disadvantages.

Analysis of microstructure images can yield an enormous amount of information about a material! For example, some alloys exhibit a dendritic structure characterized by the presence of myriad snow-flake-like dendrites that form during the solidification process of casting molten metals. Dendrites can form when the interface of the solid cast and the liquid alloy has a lower temperature as compared to the remaining melt resulting in a temperature gradient known as constitutional

Correspondence: sparks@eng.utah.edu

undercooling (Hurle 1961). Since dendrites can modify the mechanical properties in beneficial or detrimental ways, (Wang, Lee, and Mclean 2003) it is important to classify microstructures of materials as dendritic and non-dendritic.

Traditionally, humans have leveraged training and extensive domain knowledge to interpret and categorize microscopy images. This poses challenges for interdisciplinary research as well as automated, human-out-of-the-loop experimentation. Moreover, even highly trained humans are still prone to errors and bias during materials characterization. This gave rise to the implementation of computational methods on the study of dendritic microstructures which started back in 1998 to focus on the evolution of the said microstructures using phase-field modeling (Provatas, Goldenfeld, and Dantzig 1998). Later attempts have been made on three-dimensional reconstruction of microstructures captured from different microscopes which have helped in getting better insights about the mechanical properties (Alkemper and Voorhees 2001; Uchic 2011). But all these works were simulation-based and time-consuming.

An alternative to physics-based models is statistical, data-driven models that trade accuracy for speed by leveraging correlations and patterns in data. Machine learning models have been used extensively to analyze various microstructural morphologies over the last two decades(Yang et al. 2021). One such example is the development of optimal morphology derivation from a given microstructure using Bayesian optimization and kinetic Monte Carlo simulation(Tran et al. 2020). Transfer learning has been deployed for microstructure reconstruction and structure-property predictions (Li et al. 2018) while support vector regression and multi-layer perceptron (MLP) is used to predict information related to dendrite formation to improve high-temperature creep and fatigue resistance (Jiang et al. 2018). Different types of industry-relevant titanium alloy microstructures can now be classified using convolution neural networks (Baskaran et al. 2020). A particle swarm optimization algorithm has been deployed to classify the casting techniques resulting in dendritic and non-dendritic microstructures in aluminum metal matrix composites (Shabani et al. 2015). Advanced computer vision techniques have even been utilized to generalize microstructure morphology classification beyond individual alloy systems(Chowdhury et al. 2016; Impoco and Tuminello 2015; Nikolić, Štajduhar, and Čanađija 2021).

In this work, we turn to a recently reported, nature-inspired algorithm called Binary Red Deer Algorithm (BRDA) (Fard and Hajiaghaei-Keshteli 2016) to implement feature engineering to classify microstructural morphologies as dendritic or non-dendritic. For reference, we also present a comparative study between the transfer learning approach and the BRDA feature engineering approach in classifying microstructural morphologies. We show that BRDA outperforms advanced transfer learning techniques and has promise in the evolving field of computer vision in materials informatics.

2 Methodology

The dataset and code used for this work and as described in the following sections are available at **https://github.com/stochasticmaterialism/Dendritic-Non-Dendritic-Classification**.
An image dataset consisting of two different types of micrographs, dendritic and non-dendritic, has been considered in this work. The number of images in the dendritic class is 133 while that in the non-dendritic class is 444 which is quite low from a machine learning standpoint. Consequently, we have performed data augmentation on this dataset by rotating the images at various angles which have given us a six-fold increase in the number of images per class. The number of images after data augmentation in the dendritic and non-dendritic classes are 931 and 3108, respectively.

Following this, we have used transfer learning and feature engineering approaches as elaborated in subsection 2.3 and subsection 2.4 respectively to develop binary image classification models on the augmented dataset.

2.1 Dataset

The dataset has been built using the Dissemination of Information Technology for Promotion of Materials Science (DoITPoMS), a web-based initiative that started in the Materials Science and Metallurgy Department at Cambridge University (Barber, Leake, and Clyne 2007). DoITPoMS comprises a collection of micrographs covering a wide range of specimen types like ceramic, metal or alloy, device, composite, polymer, foam, etc., and microscopy techniques like optical micrography, SEM, or TEM. Information related to chemical composition and processing technique is also available as metadata for every microstructure. Additionally, in some cases, microstructures corresponding to a particular specimen are available at different magnifications. We have collected a total of 577 micrographs across 21 different alloy systems and based on their morphologies, we have divided them into two categories, dendritic and non-dendritic comprising 133 and 444 images respectively. Using these 577 micrographs, we have prepared training and test sets. The training set consists of 93 dendritic and 310 non-dendritic micrographs while the test set comprises 40 dendritic and 134 non-dendritic micrographs. This proposed work aims to develop a binary image classification model that can distinguish microstructures having dendritic morphology from non-dendritic ones. Figure 1 shows some example images used to build the proposed binary classification models.

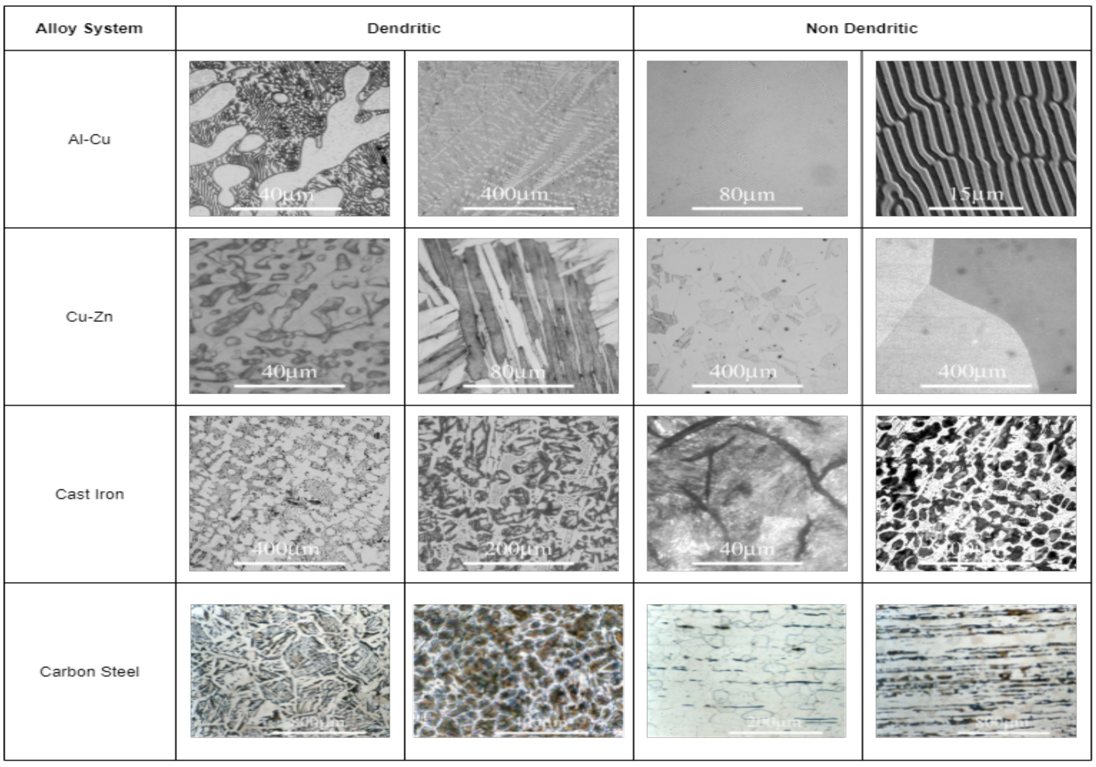

Figure 1: Example micrographs considered in this work.

2.2 Data Preprocessing

At first the micrographs are converted to single channel, i.e., grayscale format from three-channel RGB format using `BGRtoGRAY` function available in `OpenCV 4.5.3` (Bradski and Kaehler 2008) library. Each micrograph has a scale bar at the bottom indicating the magnification at which it has been recorded. The scale bars are not a part of the morphologies of the micrographs and have no significant information towards the classification objective. Consequently, the scale bar potion has been removed by cropping the grayscale micrograph followed by down-sampling to a dimension of 300×300. This ensures a uniform 300×300 parameter matrix for all the images present in the dataset without encountering any information loss. The down-sampled micrographs are augmented using `ImageDataGenerator` function available in `Keras 2.4.0` (Géron 2019) to increase the number of images in order to achieve better classification results. Each micrograph is rotated at five different angles, 50^o, 100^o, 150^o, 200^o, 250^o, and 300^o to the original micrograph. This results in six new representations of the initial micrograph. Down-sampling, and data augmentation has been performed separately for the training and test sets to ensure that the six new versions of any micrograph belong to the set, i.e., training or test where the original micrograph is present. Figure 2 delineates the augmented images and the corresponding initial micrograph for the Cu-Ni alloy system having dendritic morphology. Data augmentation gives us a six-fold increase in the number of images with 931 micrographs in the dendritic category and 3108 micrographs in the non-dendritic category. This augmented dataset is now used to build binary image classification models to distinguish the dendritic morphologies from the non-dendritic ones.

2.3 Transfer Learning Approach

Three different pre-trained CNN architectures; `VGG-16` (Simonyan and Zisserman 2014), `InceptionV3` (Szegedy et al. 2015) and `Xception` (Chollet 2017) have been used. These networks have been trained and validated separately using the augmented dataset. At first, the transfer learning approach has been implemented to train the classification models. Initially, all the layers were frozen and the weights corresponding to training on the `ImageNet` dataset (Deng et al. 2009) were used to validate the networks on the augmented dataset. Subsequently, the Edisonian approach was followed by freezing and unfreezing different layers. For frozen layers, weights corresponding to training on the `ImageNet` dataset were used while the non-frozen layers were trained to the training set. Figure 3 and Figure 4 show the architectures along with the frozen and unfrozen layers for `VGG16` and `InceptionV3` networks, respectively, that have given the maximum validation accuracy on the augmented dataset where grey boxes indicate the frozen layers. In the case of `VGG16`, the first four convolution layers have been frozen. This is followed by three repeating units of three convolution layers separated by a max pool layer. For each of these three units, a general pattern of freezing the middle convolution layer has been observed. The remaining two fully connected layers and softmax layers have been trained on the augmented dataset. In `InceptionV3`, the first five convolution layers have been frozen. The layers at the end in the form of fully connected and softmax have been trained to our dataset. In between, we have three different types of inception modules (L_1, L_2 and L_3) where convolution layers have been frozen at random based on a trial and error approach. In the case of `Xception`, transfer learning did not prove to be efficient and all the layers were trained on the augmented dataset.

For each of these network, the batch size is kept 2827 which is equal to the size of the training set. This ensures that at every iteration during training, all the entire training set used. Four different optimizers were used for each of the three networks, `Nesterov Accelerated Gradient (NAG)` (Dozat 2016), `Adagrad` (Lydia and Francis 2019), `RMSprop` (Mukkamala and Hein 2017), and `ADAM` (Zijun Zhang 2018). Training has been performed separately considering these four optimizers for

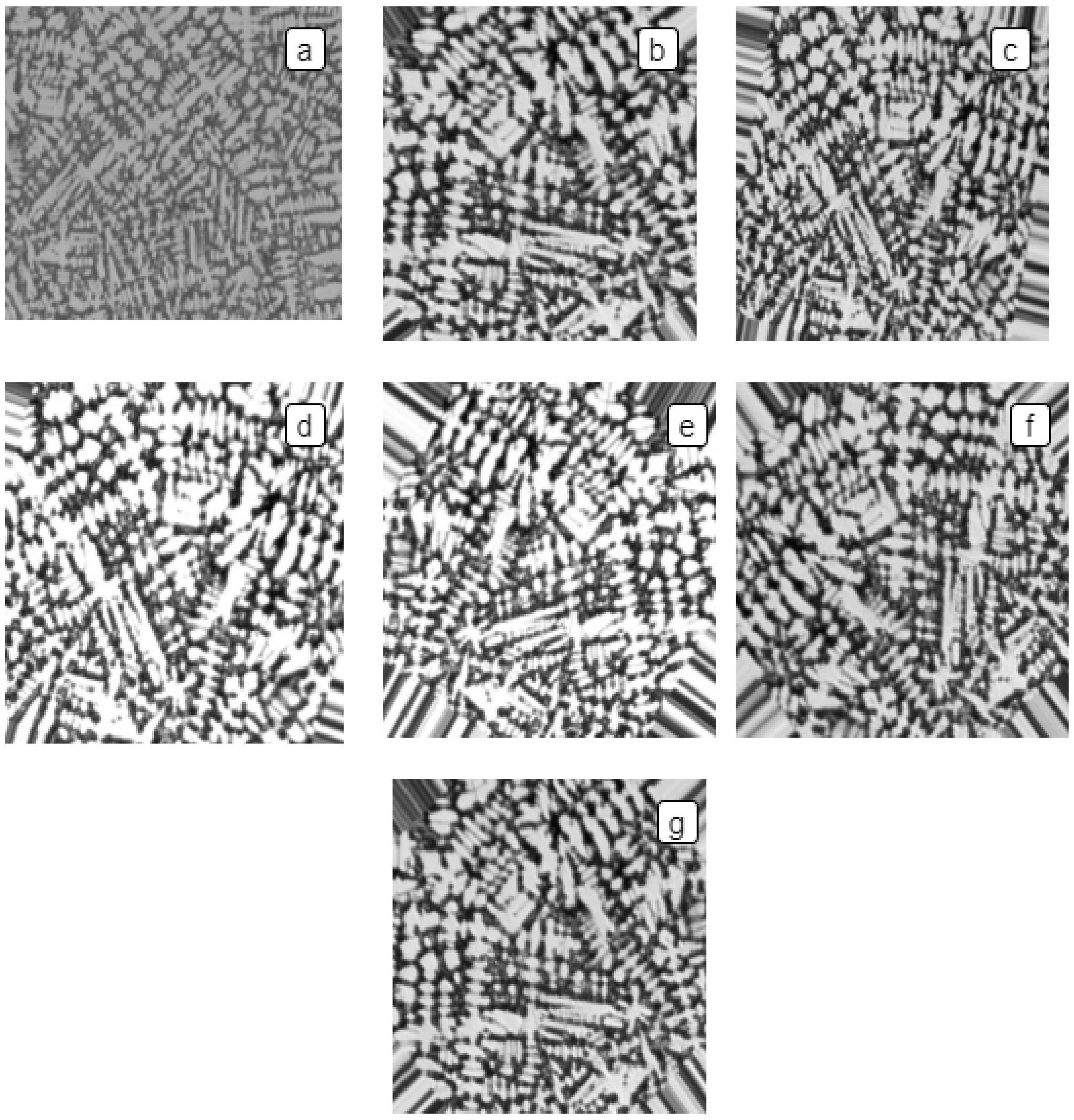

Figure 2: Figure showing (a) The down-sampled micrograph and (b)-(g) The augmented images obtained by rotating the initial micrograph at six different angles of Cu-Ni alloy system

all three networks. Hyperparameter tuning was performed for each of these optimizers for all three networks to determine the optimum value of learning rate. Loss function is set as `categorical cross entropy (CCE)` (Zhilu Zhang and Sabuncu 2018). The best validation accuracies by validating on the test set obtained for `VGG16`, `InceptionV3` and `Xception` considering the discussed architectures are 0.8313, 0.8688 and 0.8594 respectively.

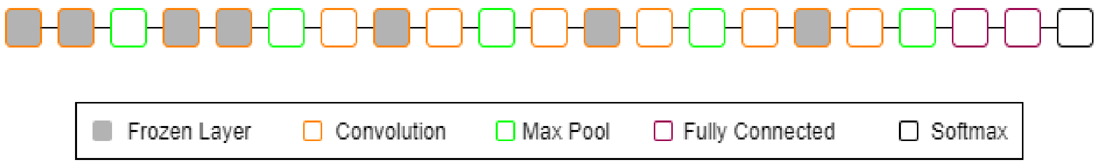

Figure 3: Architecture of `VGG16` network depicting the frozen and unfrozen layers

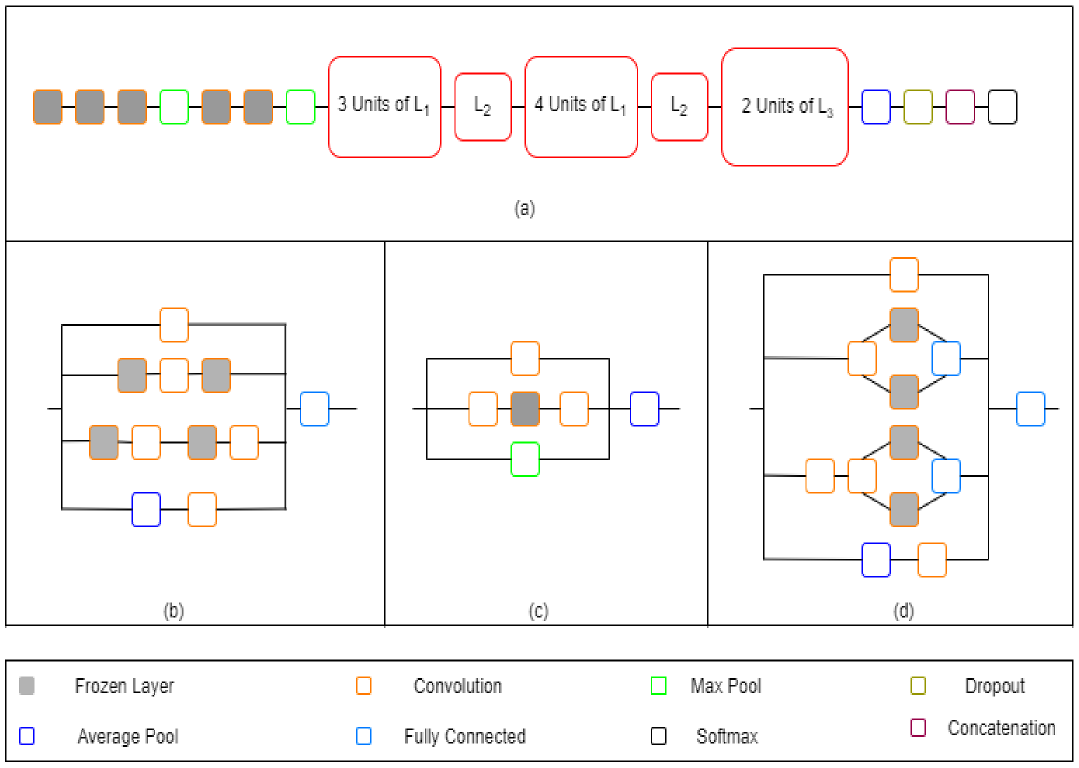

Figure 4: Schematic diagram showing (a) Architecture of `Inception3` network depicting the frozen and unfrozen layers, (b) `Inception` module 1 (L_1), (c) `Inception` module 2 (L_2) and (d) `Inception` module 3 (L_3)

2.4 Feature Engineering Approach

Since `InceptionV3` has given the maximum validation accuracy among the three pre-trained networks, it is used as a feature extractor on the training and test sets separately. This gives 12,289 features per image. This feature set corresponding to the training set is used to train two machine learning classifiers, random forest (RF) (Breiman 2001) and MLP (Gardner and Dorling 1998). The F1 scores of classification as obtained on the feature set corresponding to the test set for RF and MLP are 0.488 and 0.598 respectively. To improve upon the classification results, a meta-heuristic optimization algorithm, BRDA (Fathollahi-Fard, Mostafa Hajiaghaei-Keshteli, and Tavakkoli-Moghaddam 2020), has been deployed on the feature set of the training set. BRDA reduces the size of the feature vector to 6072 features per image. The indices of the features retained in the optimized feature set corresponding to the training set is used to optimized the feature set of the test set. Following this feature selection, RF and MLP have been trained on the optimized feature set of the test set and the F1 scores on the optimized test feature set for RF and MLP are 0.963 and 0.969 respectively. BRDA has been delineated in subsection 2.5.

2.5 Binary Red Deer Algorithm (BRDA)

Red Deer Algorithm (RDA) is a recently proposed nature-inspired meta-heuristic optimization algorithm (Fazli, Fathollahi-Fard, and Tian 2019) which is derived from the mating behavior of a sub-species of red deer known as Scottish red deer. During a breeding season, the male red deer (RD) begin the mating ritual by roaring which attracts the female counterparts called hinds. These male RDs' are categorized as commanders, ones having higher roaring intensity, and the rest are called stags. Every commander forms a harem, a group of hinds that mate with that particular commander. Harem size depends on the power of the commander defined by its fitness value. Besides, a commander also can mate with hinds belonging to other harems. Stags, on the other hand, mate randomly with their nearest hinds. This phenomenon of mating ensures a competitive evolution at each stage of the algorithm which explores the entire space of RDs'. In this work, we aim to use a binarized form of RDA called Binary Red Deer Algorithm (BRDA) for feature selection to choose an optimized subset of features from the whole set of features obtained from the augmented dataset using InceptionV3. The aim here is to maximize the classification accuracy simultaneously minimizing the number of features. Therefore, in this work, feature selection is modeled as a binary optimization problem, where the solutions are limited to {0,1}. In the BRDA, we first randomly initialize a vector of real numbers called RD of size m, the total number of features in the feature set.

$$RD = [X_1, X_2, X_3, ..., X_m] \tag{1}$$

RD is converted into a binary vector (BRD) comprising only 0 and 1 using the Sigmoid function shown in Equation 2. Here 1 indicates that the corresponding feature is selected in the feature subset and vice versa for 0. The real values of RD are converted into binary values using a threshold of 0.5 as expressed in Equation 3.

$$S(x) = \frac{1}{1+e^{-x}} \tag{2}$$

$$X_i = \begin{cases} 1 & \text{if } S(X_i) > 0.5 \\ 0 & \text{if } S(X_i) \leq 0.5 \end{cases} \tag{3}$$

where $i \in [1, m]$. The quality of the RDs at every iteration of the algorithm is evaluated by a fitness function as expressed in Equation 12.

2.5.1 Initialization of RD population

At first, an RD population of size N is initialized randomly. Based on fitness values, the top RDs represent the males (N_1), and the rest of the RDs represent the hinds (N_2). The fraction of the RD to be considered as male is a hyperparameter for BRDA and needs to be specified manually.

2.5.2 Roaring male RDs

To successfully roar and attract hinds, the male RDs may change their positions according to Equation 4. If the fitness value of the male RDs at the new position is better than that in the original position, then the position of the RD is updated and roaring is considered to have been successful. Otherwise, the old position is retained.

$$new = \begin{cases} old + a_1 \times ((upper - lower) \times a_2 + lower) & if\, a_3 \geq 0.5 \\ old - a_1 \times ((upper - lower) \times a_2 + lower) & if\, a_3 < 0.5 \end{cases} \tag{4}$$

Here, *old* is the original position of the male RD whereas *new* is the position to which a male RD moves during the roaring procedure. a_1, a_2 and a_3 are randomly generated numbers from a uniform distribution of 0 and 1 while $upper = 1$ and $lower = -1$ are the upper and lower bounds of the search space of the entire RD population.

2.5.3 Distinguishing Commanders from Stags

Among the male RDs, the top N_3 are selected as commanders according to Equation 5

$$N_3 = floor\,(\gamma \times N_1) \tag{5}$$

where $\gamma \in [0, 1]$ is a hyperparameter which is to be specified manually. Each of these commanders competes with the $N_1 - N_3$ number of stags randomly and two new solutions, New_1 and New_2 are generated as expressed in Equation 6 and Equation 7 respectively. The position of the commander is updated using the solution which results in the best fitness value among the commander, the stag, and the two new solutions.

$$New1 = \frac{Commander + Stag}{2} + (b_1 \times ((upper - lower) \times b_2) + lower) \tag{6}$$

$$New2 = \frac{Commander + Stag}{2} - (b_1 \times ((upper - lower) \times b_2) + lower) \tag{7}$$

$Commander + Stag$ represents addition of the two vectors corresponding to commander and stag respectively. b_1 and b_2 are generated using a uniform distribution function in [0,1].

2.5.4 Formation of Harems

Since this is a minimization problem, better quality of solution is determined by a lower fitness value. Therefore, we find the power of each commander according to Equation 8

$$P_j = F - f_j \tag{8}$$

where P_j and f_j are the power and fitness value of the jth commander respectively and $j \in [1, N_3]$. F is the sum of fitness values of all commanders. Equation 9 represents the fraction of the total number of hinds that form a harem with a particular commander.

$$N_{4_j} = floor\,\{P_j \times N_2\} \tag{9}$$

where N_{4_j} is the number of hinds that belongs to the jth harem.

2.5.5 Mating of Commanders

In each harem, all hinds mate with the respective commander to produce offspring according to Equation 10.

$$offspring = \frac{Commander + Hind}{2} + (upper - lower) \times c \tag{10}$$

Here c is a randomly generated number between 0 and 1. Besides, all the commanders can mate with hinds from all other harems. Consequently, a new population of RDs is generated which are stored in *offspring pool*

2.5.6 Mating of Stags

Each stag mates with its nearest hind irrespective which of harem the hind belongs to. The distance between a stag and all hinds is calculated by Equation 11.

$$d_k = \sqrt{\sum_{k \in N_2} \left(stag_k - hind_k^j \right)^2} \tag{11}$$

where d_k is the distance between a stag and the jth hind. The hind at the minimum distance is selected for mating, which takes place according to Equation 10, with the stag replacing the male commander. The offspring formed in this process are added to the *offspring pool.*

2.5.7 Selection of Next Generation

After the mating process is completed, the offspring from the *offspring pool* are shuffled with the original population. The top N RDs are selected according to fitness values as the next generation and the rest of the solutions are discarded.

2.5.8 Terminating the BRDA

The process is stopped when *iter* number of iterations are completed. The RD with the best fitness value in the final generation represents the optimized feature subset which is used to train the RF and MLP classifiers.

2.5.9 Fitness Evaluation

Fitness quantifies the quality of the BRDA solution. A learning algorithm based on an RF classifier is used to evaluate the performance of a particular feature subset along with the whole feature set. The fitness function consists of two components: classification accuracy and the number of features. Our objective is to achieve the highest classification accuracy minimizing the number of features. Higher classification accuracy and fewer features imply a low fitness value. The fitness function is shown in Equation 12.

$$Fitness = \kappa \times \frac{|Selected|}{|Total|} + (1 - \kappa) \times \psi \tag{12}$$

where $|Selected|$ is the number of features in the selected feature subset, $|Total|$ is the total number of features of the dataset, ψ is the classification error of the feature subset, and $\kappa \in [0, 1]$ indicates the relative weight assigned to the number of features and the classification error.

The time complexity of BRDA is expressed as $O(iter * N^2 * (t + m))$ where t is the time complexity in calculating the fitness of a particular RD using the RF classifier.

3 Results and Discussion

The code to build the transfer learning and feature engineering-based models have been developed predominantly by using two Python libraries, `TensorFlow Core v2.5.0` and `Scikit-Learn 0.24.2`. The optimal learning rate for each of the four optimizers: NAG, Adagrad, RMSProp, and ADAM is determined experimentally on a trial and error basis. Figure 5 shows the variation of validation accuracy with the learning rate for all four optimizers across all three network architectures as elaborated in subsection 2.3. Using NAG optimizer, the validation accuracies for VGG16

Algorithm 1 Algorithm of BRDA

```
Input: $iter$, $N$
Output: Optimized feature set $X' = (x_1, x_2, ..., x_m)$
  Initialize RD population
  Determine $N_1$ males and $N_2$ hinds based on fitness of RDs
  for $e_1 \leftarrow 1$ to $iter$ do
      for $e_2 \leftarrow 1$ to $N_1$ do
          Update position of RD if fitness increases
      end for
      Level stags and commanders
      for $e_2 \leftarrow 1$ to $N_3$ do
          Competition between commander and stag
          Update position of the commander
      end for
      Creation of harems
      for $e_2 \leftarrow 1$ to $N_3$ do
          Mating commander with hinds from its harem
          Mating commander with hinds from other harems
      end for
      for $e_2 \leftarrow 1$ to $(N_1 - N_3)$ do
          Select the closest hind from the nearest harem
          Mating of stag with the selected hind
      end for
      Selection of the next generation from offspring pool
      Update $X'$ if a better solution is encountered
  end for
  return $X'$
```

and Xception decrease continuously starting from 0.74 and 0.81 respectively whereas the same for InceptionV3 increases continuously up to 0.77. This shows that the NAG optimizer is most efficient in the case of Xception. Using Adagrad optimizer, there is a continuous decrease in the validation accuracies for Xception and vice versa for VGG16 and InceptionV3. But InceptionV3 shows predominantly higher validation accuracies as compared to VGG16 and Xception particularly when the learning rate is between 0.02 and 0.42. Using RMSProp optimizer, similar trends are observed in cases of InceptionV3 and Xception where the validation accuracies increase up to a maximum value followed by a sharp decrease while a reverse trend is observed in the case of VGG16. However, InceptionV3 has predominantly had higher validation accuracies as compared to VGG16 and Xception. Using ADAM optimizer, InceptionV3 and Xception show irregular trends while VGG16 has a parabolic decrement in validation accuracies to the learning rate. However, the maximum validation accuracies obtained with the ADAM optimizer for all three networks surpasses the maximum accuracies obtained with the remaining three optimizers as shown in Figure 6.

Therefore, transfer learning with the proposed network architectures as delineated in subsection 2.3 using the ADAM optimizer provided the best micrograph classification results with validation accuracies equal to 0.8313, 0.8688, and 0.8594 for VGG16, InceptionV3, and Xception respectively where the learning rates for the ADAM optimizer are 0.027, 0.339 and 0.007 for VGG16, InceptionV3 and Xception respectively. Early stopping has been deployed in the case of training the pre-trained networks to minimize the number of epochs and obtain the optimum results (Prechelt

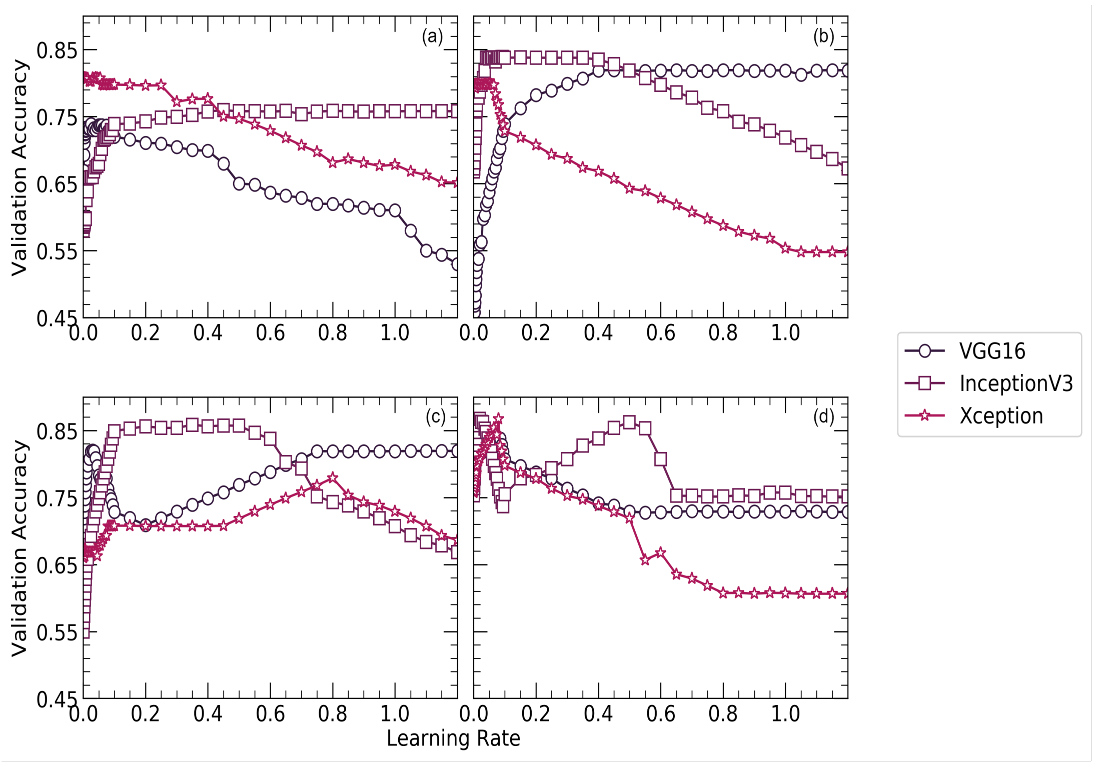

Figure 5: Plots showing the variation of validation accuracy with learning rate using (a) `NAG`, (b) `Adagrad`, (c) `RMSProp` and (d) `ADAM` optimizers for all three networks

1998). Consequently, `VGG16`, `Inception3` and `Xception` were stopped after 35, 37, and 43 epochs, respectively using the ADAM optimizer where the training failed to reach any maxima beyond this point. Figure 7 delineates the epoch-wise training accuracies, validation accuracies, CCE training loss, and CCE validation loss for each of the three networks. Early stopping gives us validation accuracies of 0.8313, 0.8688 and 0.8594 as shown in Figure 6 and validation losses of 0.3, 0.27 and 0.28 for VGG16, Inception3 and Xception respectively and the corresponding training accuracies for these networks are 0.9819, 0.9997 and 0.9856 while the training losses are 0.1, 0.04 and 0.045 respectively as shown in Figure 8. These results indicate that even the best combination and frozen and unfrozen layers fail to provide a generalized binary classifier due to overfitting.

BRDA used for feature optimization has several parameters as shown in Table 1 which need to be specified at the start of the algorithm. The optimum values of these parameters have been determined experimentally following a trial and error approach. Each of these parameters has been plotted to the corresponding accuracies obtained by the RF and MLP classifiers as shown in Figure 9. From the independent plots, we can determine the optimum values of these parameters. While determining a particular parameter, the remaining parameters are set to arbitrary values. This implies that each of these parameters if set to their optimum values, can alone provide a nearly optimized subset which can lead to accurate classification results which are close to the actual classification results when all the parameters with their optimum values are combined. Therefore, a single parameter itself can bring a significant change to the entire model performance and param-

Figure 6: The maximum validation accuracy and the corresponding learning rate obtained from using `NAG`, `Adagrad`, `RMSProp` and `ADAM` optimizers for all three networks

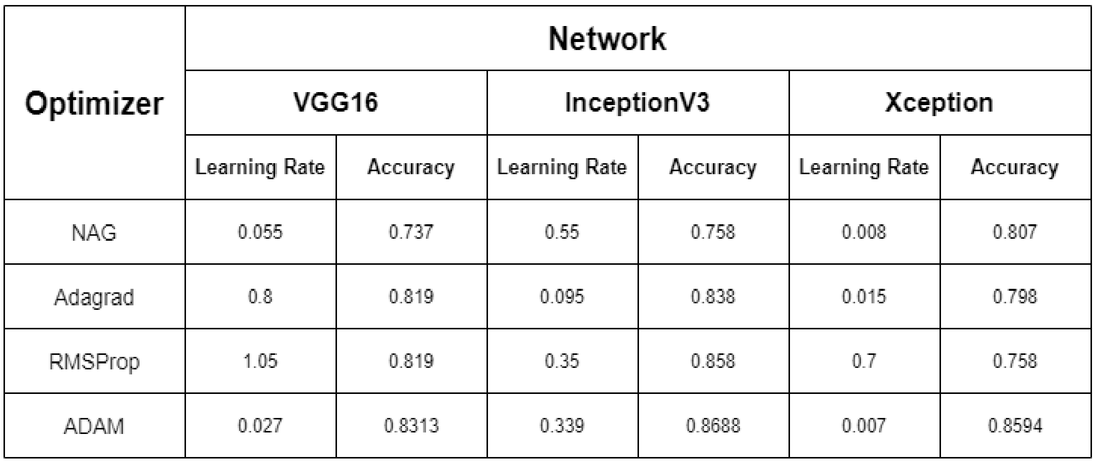

Optimizer	**Network**					
	VGG16		**InceptionV3**		**Xception**	
	Learning Rate	Accuracy	Learning Rate	Accuracy	Learning Rate	Accuracy
NAG	0.055	0.737	0.55	0.758	0.008	0.807
Adagrad	0.8	0.819	0.095	0.838	0.015	0.798
RMSProp	1.05	0.819	0.35	0.858	0.7	0.758
ADAM	0.027	0.8313	0.339	0.8688	0.007	0.8594

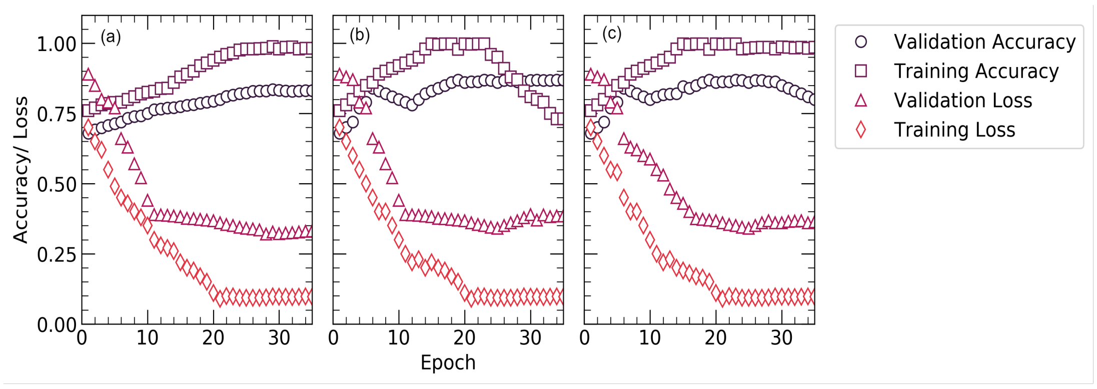

Figure 7: Plots showing the performance of (a) `VGG16`, (b) `InceptionV3` and (c) `Xception` networks on the augmented dataset

eter tuning becomes an important step of experimentation.

Without BRDA, RF and MLP give poor classification results with accuracies of 0.4198 and 0.5556, respectively. As shown in Figure 10, the area under the ROC curves (AUC) for each of these classifiers without using BRDA are 0.478 and 0.532 respectively. These poor values of classification metrics are an indication of improper classification of dendritic and non-dendritic micrographs which can be seen from the true positive rate (TPR) and false-positive rate (FPR) values as shown in Figure 11. TPR values are 0.4987 and 0.5073 and those of FPR are 0.775 and 0.8743 for RF and MLP classifiers respectively without using BRDA. However, after deploying the BRDA feature optimization algorithm, we note a drastic improvement in the classification results with accuracies

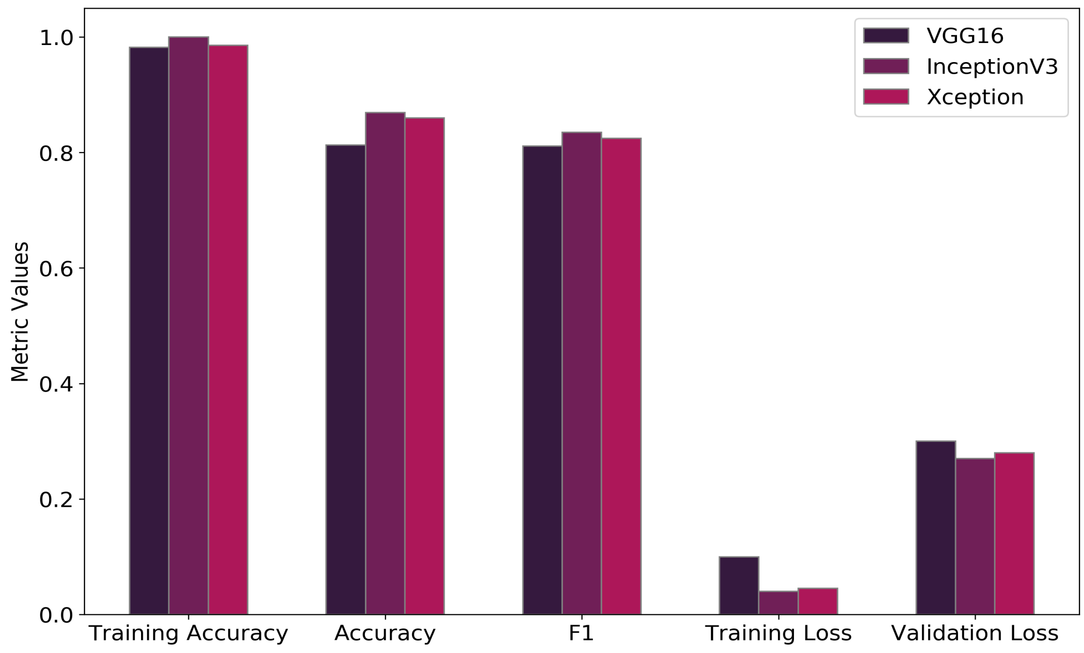

Figure 8: Comparison between the accuracies and CCE losses for training and validation of the final pre-trained network architectures

of 0.9735 and 0.9855 and AUC of 0.97 and 0.979 for RF and MLP classifiers respectively. Besides, the F1 scores for RF and MLP classifiers are 0.963 and 0.969 respectively after the implementation of BRDA in contrast to the same without BRDA which are 0.488 and 0.598 respectively. On the contrary, the F1 scores for VGG16, InceptionV3 and Xception network architectures as delineated in subsection 2.3 are 0.811, 0.835 and 0.8246 respectively using the ADAM optimizer. The F1 scores indicate that applying BRDA reduces the number of images falsely classified as the other category significantly. Figure 11 gives a comparative plot depicting the classifier evaluation metrics before and post-implementation of BRDA. It has been established from the FPR values that the number of microstructural images which were incorrectly classified without using BRDA has reduced significantly. FPR post-implementation of BRDA are 0.39 and 0.25 for RF and MLP respectively. Figure 10 provides a better understanding of the performance of the classifiers with and without BRDA with the help of ROC curves.

Therefore, feature optimization using BRDA and using classical machine learning classifiers have proven to be more efficient in characterizing micrographs as dendritic or non-dendritic as compared to transfer learning. The classification results using BRDA have been compared using standard feature selection algorithms available in `Scikit-Learn 0.24.2` library. We have compared our results with recursive, L1-based, and tree-based feature selection methods for both RF and MLP classifiers. Figure 12 shows the variation of F1 scores for RF and MLP classifiers when BRDA and other feature selection algorithms are deployed. F1 scores obtained by using recursive, L1-based, and tree-based feature selection algorithms for RF classifiers are 0.763, 0.781, and 0.831 respectively while the same on MLP classifiers are 0.788, 0.807, and 0.84 respectively. In contrast to the F1 scores

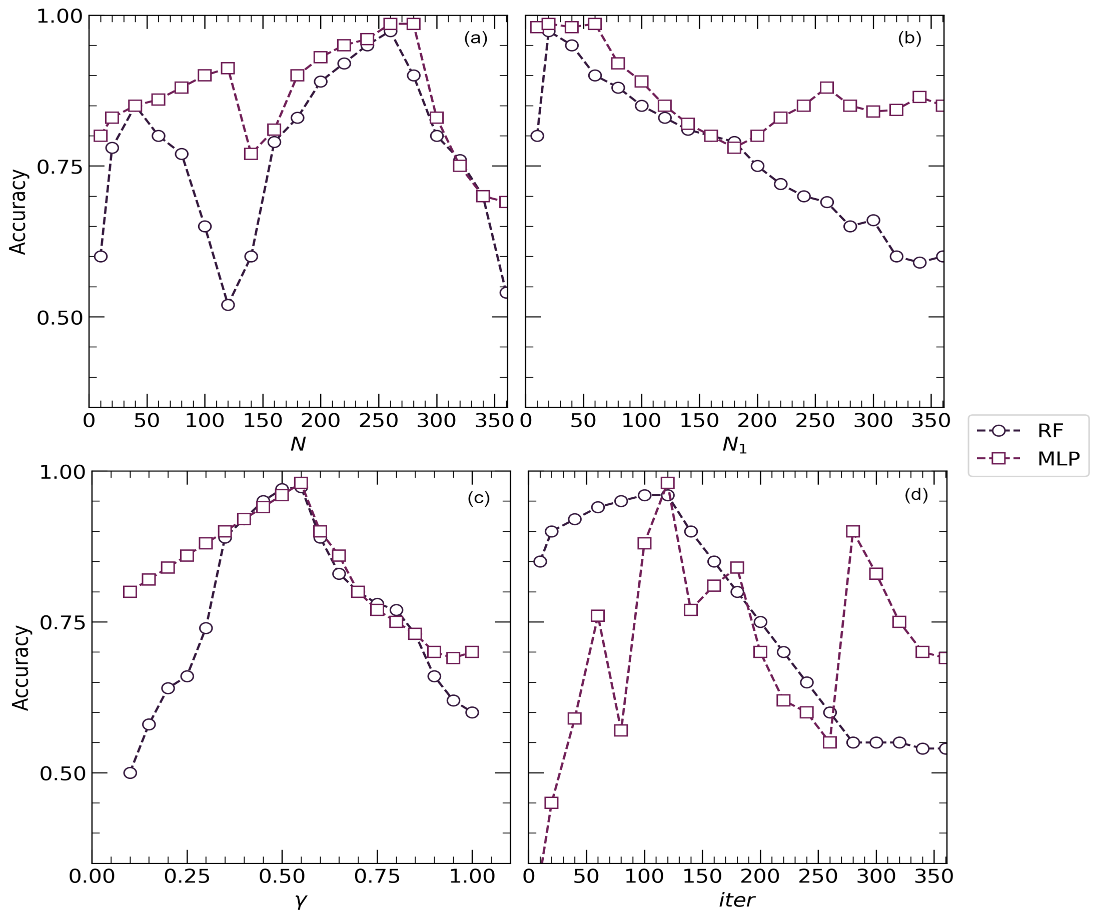

Figure 9: Experimental determination of the parameters of BRDA (a) RD population (N) (b) Number of male RDs (N_1) (c) Ratio of the number of commanders to total number of male RDs (γ) and (d) Total number of iterations for which BRDA is executed (iter)

obtained for RF and MLP upon using BRDA which are 0.963 and 0.969 respectively, other feature selection algorithms have less efficient in classifying micrographs as dendritic or non-dendritic.

4 Conclusion

This work focuses on a comparative study between transfer learning and feature engineering approaches in the classification of dendritic and non-dendritic microstructural morphologies. Transfer learning using `VGG16`, `InceptionV3` and `Xception` fails to provide proper generalization in microstructural characterization. Consequently, we have utilized a feature engineering approach using a meta-heuristic optimization algorithm called Binary Red Deer Algorithm which improves the performances of two machine learning classifiers drastically. Parameter tuning plays an important role in the optimization of the feature set and therefore impacts the classification results in turn. This work provides an uncommon example of where feature engineering has outperformed transfer learning. Besides, BRDA also has better feature selection ability as compared to some standard

Table 1: Optimal parameter settings of the proposed FS method called BRDA

Parameter	**Meaning**	**Value**
N	RD population	260
N_1	Number of male RDs	20
γ	Ratio of the number of commanders to the total number of male RDs	0.57
iter	Total number of iterations for which BRDA is executed	120

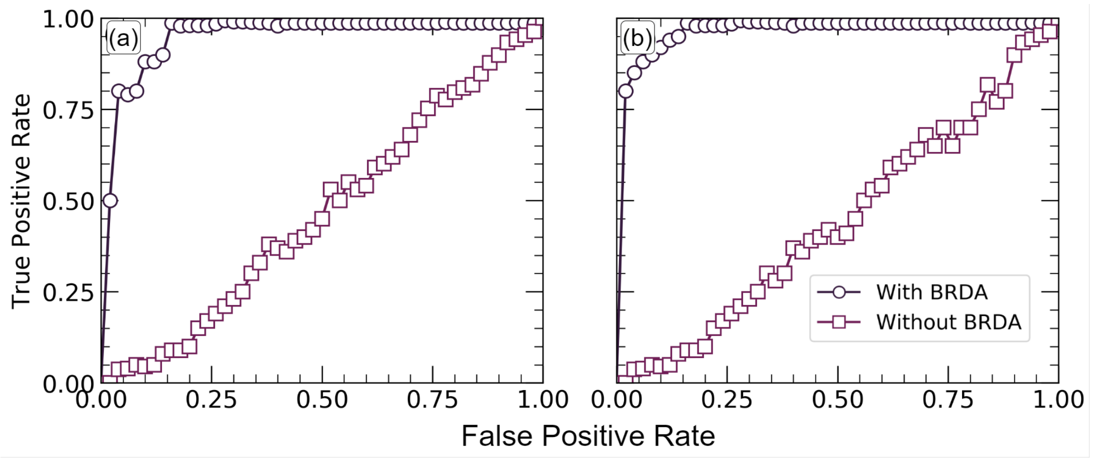

Figure 10: Performance of (a) RF and (b) MLP classifiers with and without using BRDA

feature selection algorithms available in `Scikit-Learn 0.24.2`. However, this work is restricted to 21 different alloys systems. Extending the implementation of BRDA beyond these 21 alloys systems and even to other materials will be our future aim. BRDA, therefore, brings significant promise in the field of materials informatics and we will aim to extend its use beyond materials characterization in future contributions.

Acknowledgements
The authors gratefully acknowledge support from the NSF CAREER Award DMR 1651668. Special thanks to Sterling Baird for his helpful comments and suggestions. The authors thank the creators of DoITPoMS for the creation of the microstructure databases used in this work. In addition, the authors express their gratitude to the open-source software community, for developing the excellent tools used in this research, including but not limited to Python, Pandas, NumPy, matplotlib, scikit-learn, and PyTorch.

CRedit Author Statement
Taylor D. Sparks: conceptualization, funding acquisition, project administration, supervision, writing - review and editing, visualization, validation, and formal analysis. **Debanshu Banerjee:** methodology, software, formal analysis, investigation, resources, data curation, writing - original draft.

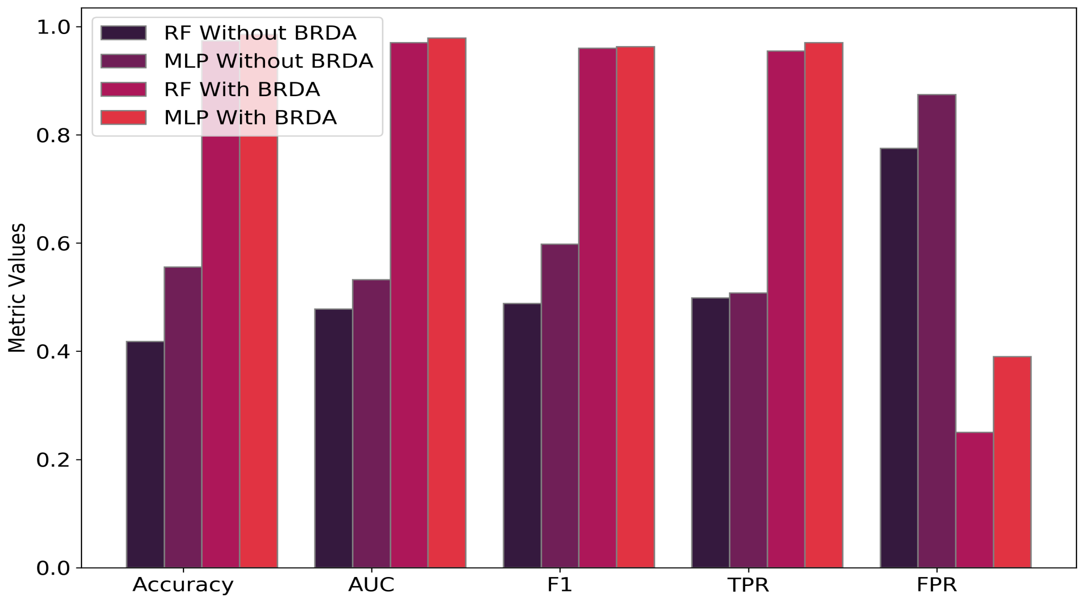

Figure 11: Comparison between the accuracies of RF and MLP classifiers with and without using BRDA

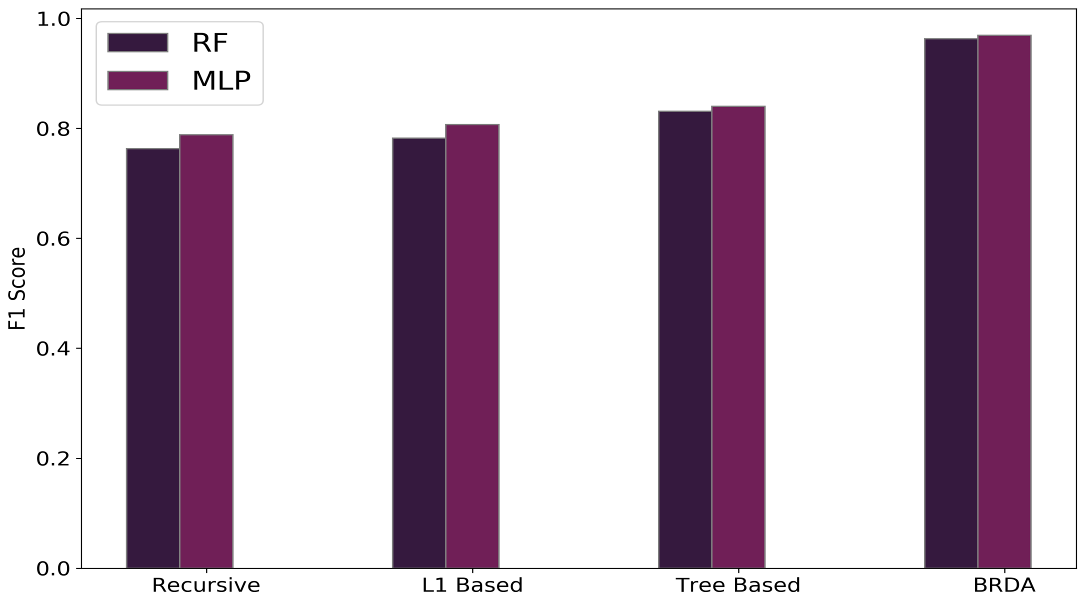

Figure 12: Comparison between the F1 scores of RF and MLP classifiers using BRDA and other feature selection algorithms

Declaration of Interests
All the authors declare that they have no conflict of interest or competing interests.

Code and Data Availability:
The The dataset and code used for this work and as described in this paper is available at **https://github.com/stochasticmaterialism/Dendritic-Non-Dendritic-Classification**

References

Alkemper, J and PW Voorhees (2001). "Three-dimensional characterization of dendritic microstructures". In: *Acta materialia* 49.5, pp. 897–902.

Barber, ZH, JA Leake, and TW Clyne (2007). "The DoITPoMS Project-a web-based initiative for teaching and learning materials science". In: *Journal of Materials Education* 29.1/2, p. 7.

Baskaran, Arun et al. (2020). "Adaptive characterization of microstructure dataset using a two stage machine learning approach". In: *Computational Materials Science* 177, p. 109593.

Bradski, Gary and Adrian Kaehler (2008). *Learning OpenCV: Computer vision with the OpenCV library.* " O'Reilly Media, Inc."

Breiman, Leo (2001). "Random forests". In: *Machine learning* 45.1, pp. 5–32.

Chollet, François (2017). "Xception: Deep learning with depthwise separable convolutions". In: *Proceedings of the IEEE conference on computer vision and pattern recognition*, pp. 1251–1258.

Chowdhury, Aritra et al. (Oct. 2016). "Image driven machine learning methods for microstructure recognition". In: *Computational Materials Science* 123, pp. 176–187. DOI: `10.1016/j.commatsci.2016.05.034`. URL: `https://doi.org/10.1016/j.commatsci.2016.05.034`.

Deng, Jia et al. (2009). "Imagenet: A large-scale hierarchical image database". In: *2009 IEEE conference on computer vision and pattern recognition.* Ieee, pp. 248–255.

Dozat, Timothy (2016). "Incorporating nesterov momentum into adam". In:

Fard, AF and M Hajiaghaei-Keshteli (2016). "Red Deer Algorithm (RDA); a new optimization algorithm inspired by Red Deers' mating". In: *International Conference on Industrial Engineering, IEEE.* Vol. 12, pp. 331–342.

Fathollahi-Fard, Amir Mohammad, Mostafa Hajiaghaei-Keshteli, and Reza Tavakkoli-Moghaddam (2020). "Red deer algorithm (RDA): a new nature-inspired meta-heuristic". In: *Soft Computing* 24.19, pp. 14637–14665.

Fazli, Masoud, Amir Mohammad Fathollahi-Fard, and Guangdong Tian (2019). "Addressing a coordinated quay crane scheduling and assignment problem by red deer algorithm". In: *International Journal of Engineering* 32.8, pp. 1186–1191.

Gardner, Matt W and SR Dorling (1998). "Artificial neural networks (the multilayer perceptron)—a review of applications in the atmospheric sciences". In: *Atmospheric environment* 32.14-15, pp. 2627–2636.

Géron, Aurélien (2019). *Hands-on machine learning with Scikit-Learn, Keras, and TensorFlow: Concepts, tools, and techniques to build intelligent systems.* O'Reilly Media.

Hurle, DTJ (1961). "Constitutional supercooling during crystal growth from stirred melts—I: Theoretical". In: *Solid-State Electronics* 3.1, pp. 37–44.

Impoco, G. and L. Tuminello (Nov. 2015). "Incremental learning to segment micrographs". In: *Computer Vision and Image Understanding* 140, pp. 144–152. DOI: `10.1016/j.cviu.2015.03.007`. URL: `https://doi.org/10.1016/j.cviu.2015.03.007`.

Jiang, Xue et al. (2018). "An materials informatics approach to Ni-based single crystal superalloys lattice misfit prediction". In: *Computational Materials Science* 143, pp. 295–300.

Li, Xiaolin et al. (2018). "A transfer learning approach for microstructure reconstruction and structure-property predictions". In: *Scientific reports* 8.1, pp. 1–13.

Lydia, Agnes and Sagayaraj Francis (2019). "Adagrad—an optimizer for stochastic gradient descent". In: *Int. J. Inf. Comput. Sci* 6.5.

Mukkamala, Mahesh Chandra and Matthias Hein (2017). "Variants of rmsprop and adagrad with logarithmic regret bounds". In: *International Conference on Machine Learning*. PMLR, pp. 2545–2553.

Nikolić, Filip, Ivan Štajduhar, and Marko Čanađija (2021). "Casting Microstructure Inspection Using Computer Vision: Dendrite Spacing in Aluminum Alloys". In: *Metals* 11.5, p. 756.

Prechelt, Lutz (1998). "Early stopping-but when?" In: *Neural Networks: Tricks of the trade*. Springer, pp. 55–69.

Provatas, Nikolas, Nigel Goldenfeld, and Jonathan Dantzig (1998). "Efficient computation of dendritic microstructures using adaptive mesh refinement". In: *Physical Review Letters* 80.15, p. 3308.

Shabani, Mohsen Ostad et al. (2015). "Refined microstructure of compo cast nanocomposites: the performance of combined neuro-computing, fuzzy logic and particle swarm techniques". In: *Neural Computing and Applications* 26.4, pp. 899–909.

Simonyan, Karen and Andrew Zisserman (2014). "Very deep convolutional networks for large-scale image recognition". In: *arXiv preprint arXiv:1409.1556*.

Szegedy, Christian et al. (2015). "Going deeper with convolutions". In: *Proceedings of the IEEE conference on computer vision and pattern recognition*, pp. 1–9.

Tran, Anh et al. (2020). "An active learning high-throughput microstructure calibration framework for solving inverse structure–process problems in materials informatics". In: *Acta Materialia* 194, pp. 80–92.

Uchic, Michael D (2011). "Serial sectioning methods for generating 3D characterization data of grain-and precipitate-scale microstructures". In: *Computational methods for microstructure-property relationships*. Springer, pp. 31–52.

Wang, W, Peter D Lee, and M_ Mclean (2003). "A model of solidification microstructures in nickel-based superalloys: predicting primary dendrite spacing selection". In: *Acta materialia* 51.10, pp. 2971–2987.

Yang, Kaiqi et al. (2021). "Self-supervised learning and prediction of microstructure evolution with convolutional recurrent neural networks". In: *Patterns* 2.5, p. 100243.

Zhang, Zhilu and Mert R Sabuncu (2018). "Generalized cross entropy loss for training deep neural networks with noisy labels". In: *32nd Conference on Neural Information Processing Systems (NeurIPS)*.

Zhang, Zijun (2018). "Improved adam optimizer for deep neural networks". In: *2018 IEEE/ACM 26th International Symposium on Quality of Service (IWQoS)*. IEEE, pp. 1–2.